On inter-element forces in the FEM-displacement formulation, and implications for stress recovery

Daniela Ciancio, Ignacio Carol, Massimo Cuomo

On inter-element forces in the FEM-displacement formulation, and implications for stress recovery

D. Ciancio[1], I. Carol[2,*,†] and M. Cuomo[1]

[1]*Dipartimento di Ingegneria Civile ed Ambientale, Universitá di Catania, Catania, Italy*
[2]*School of Civil Engineering (ETSECCPB), Technical University of Catalonia (UPC), Barcelona, Spain*

SUMMARY

This paper describes a new technique for the determination of the inter-element forces and tractions, as well as stress state at nodes, as a post-processing step after the solution of standard FE-displacement calculation. The work is motivated in the context of a broader development of a procedure to simulate fracture processes using a discrete approach without the need of double-noded interface elements. The technique, easily implementable, is based on the double minimization of an objective function, representing the error between the inter-element stress tractions and the projection of the best-fit stress tensor **T** along the planes of the interfaces converging at an element corner node. The formulation is illustrated with some basic examples in which the resulting stress tensors and inter-element forces are compared to theoretical solutions and to the results obtained by using a traditional stress average smoothing method.

KEY WORDS: fracture; interface; inter-element forces; Mohr's circle; stress recovery

1. INTRODUCTION

Since the first attempts to the numerical modelling of damage and fracture using the FEM, one of the key aspects has been how to simulate crack propagation across the domain. In early Linear Elastic Fracture Mechanics (LEFM) simulations [1] or later non-linear fracture mechanics (NLFM) implementations [2], the mesh was changing at every time step of the calculation, sometimes with an initial notch required and a moving rosette of elements always at the crack tip. Hot points in those algorithms were crack propagation direction at each new step and new crack length. The smeared approach that was developed as an alternative, although with the

*Correspondence to: Ignacio Carol, ETSECC-UPC Jordi Girona 1-3, E-08034 Barcelona, Spain.
†E-mail: ignacio.carol@upc.es

advantage of a fixed mesh, also thrived at identifying macro-crack direction among the cloud of 'cracking' Gauss points obtained, often in chaotic state of stress and strain involving thick element bands or even substantial parts of the structure (see for instance Reference [3]). More modern techniques, such as 'extended finite element method' (XFEM) and 'strong discontinuity approach' (SDA), also require the identification of a crack path line using the so-called 'tracking algorithm', which still appears to be an '*ad hoc*' procedure independent (or at least detached) from the fundamental principles of mechanics which govern the continuum behaviour, and are intrinsically limited to handling problems with one or two (or in any case very few) simultaneous propagating cracks [4, 5].

An intermediate approach proposed very early [6], but developed more efficiently only since the 1990s as computer power became commonly available [7–11], is that of considering each line in the mesh as a potential crack, evaluating inter-element forces and stresses, and allowing crack opening/sliding along those same lines as appropriate strength criteria are exceeded. Although not free of shortcomings (e.g. cracks can only develop along the initial mesh lines), at least these methods have provided a means of describing crack propagation in a fully automatic and fully integrated way with the rest of the mechanical problem, eliminating completely the need of tracking or remeshing and without any limitations on how many cracks open, close, reopen, branch or bridge.

In practice, there are two main ways to implement these techniques. One is to insert zero-thickness interface elements with double nodes along each line of the mesh (or along a subset of them providing sufficient multiplicity of fracture paths to the structure from the beginning of the analysis) [7, 9, 11]. These interfaces are assigned a high elastic stiffness which may be interpreted as the penalty coefficient necessary to evaluate stress tractions transmitted across their surface. Integration over the interface elements is advantageously performed using special integration rules with points located in between each pair of nodes; this integration procedure brings nodal decoupling and means that the obtained stress tractions may be directly related to nodal opening or closing forces between the corresponding node pair through the concept of 'contributing area' which ensues from the interface interpolation weights and geometry [12]. The procedure based on zero-thickness interfaces has led to very realistic representation of concrete and rock specimen behaviour in 2D in a variety of loading situations [13–15] even with relatively crude meshes, and to very promising results in 3D obtained recently for the cases of uniaxial tension [16, 17].

The second possibility within the approach of considering mesh lines as potential cracks consists of avoiding the use of a penalty coefficient as elastic stiffness by adopting rigid-softening interface elements. Double-noded interfaces are inserted only along those mesh lines whose tractions reach certain failure criteria. With this procedure the computational effort is reduced substantially and also the additional compliance due to elastic stiffness of interfaces is eliminated. This technique requires the evaluation of the inter-element forces (or stress tractions between elements) from the results of a standard FE analysis in order to detect the opening of an interface. However, as simple as this idea may sound, the evaluation of such forces turns out not a trivial problem and may be ill-defined at the corner nodes in 2D or at the corner and edge nodes of elements in 3D. This may explain why the existing approaches of this type in 2D are based on inter-element force evaluation and crack verification at the mid-side nodes of quadratic element sides, only location at which the computation of such forces becomes trivial [8, 18].

In essence, what follows trivially from the standard FE solution (consisting of nodal displacements, Gauss point stresses, etc.), by means of the weak equilibrium equation, is the nodal

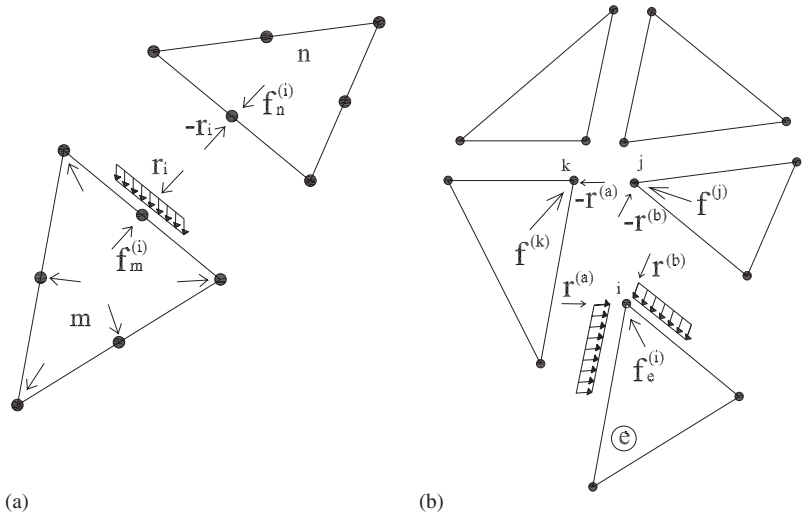

Figure 1. 2D inter-element (**r**) and nodal (**f**) forces and inter-element stress distribution for: (a) a mid-side node; and (b) a corner node.

force vector which, for a generic element e, may be expressed as

$$\mathbf{f}_e = \int_{V_e} \mathbf{B}^{\mathrm{T}} \sigma \, \mathrm{d}V \tag{1}$$

being V_e the element volume, σ the stress field in the element and $\mathbf{B}$ the matrix containing the derivatives of the element shape functions.

At intermediate nodes of the quadratic element sides, these forces (equal and opposite between adjacent elements) may be immediately identified with the inter-element forces at that point of the mesh and, using the 'contributing area concept', converted to normal/shear stresses (Figure 1(a)).

But at the corner nodes in 2D (or similarly at corner or edge nodes in 3D), these inter-element forces are not uniquely defined (or at least not by the equilibrium equations alone). This can be seen in Figure 1(b) in which the corresponding ith components of $\mathbf{f}_e$ obtained with (1) for element e give the nodal force denoted as $\mathbf{f}_e^{(i)}$ at node i, but this does not lead to a distribution of this force between $\mathbf{r}^{(a)}$ and $\mathbf{r}^{(b)}$, forces representing the stresses transmitted to the element over contributing areas of element sides a and b converging at node i, that by equilibrium must sum $\mathbf{f}_e^{(i)}$. This simple diagram already suggests that evaluation of such inter-element forces at (and, subsequently, the stress tractions near) the corner nodes, will require some additional equations or principles to break the indetermination.

To the authors' knowledge, one such procedure exists in the literature based on the geometric construction of a nodal force polygon with the inter-element forces as radial lines concurrent to an initially undetermined central point [19]. Although a valuable reference, that method includes a minimization function and weight coefficients based on geometric intuition, which seems to give reasonable results in the examples provided, but the unknown remains whether

results would be always mechanically consistent in different situations (e.g. distorted elements, 3D, etc.).

The main objective of the work described in this paper is precisely to develop a new procedure to evaluate inter-element forces at the corner nodes, with the final goal in mind of application to cracking and fracture calculations (i.e. similar to References [8, 18] but checking cracking, etc., at corner node rather than only at mid-side nodes). The new method proposed for the inter-element force determination reduces the number of non-mechanical assumptions and offers additional useful by-products. The objective function, inspired on microplane model [20], is based on the differences between inter-element forces and the projection on the same plane of a new '*nodal stress tensor*' at the node. This tensor is an additional unknown to be solved, which requires a double minimization procedure. Nevertheless, even if the analytical development becomes a little longer, the resulting equations are extremely simple and may be implemented as a mere 2×2 system to be solved at each node *a posteriori* of the standard FE analysis. The above-mentioned additional by-products of the proposed method consist of the evaluation of stress tensor at the mesh corner nodes and subsequent possible applications as advantageous stress recovery or 'smoothing' procedure.

A number of nodal stress recovery (smoothing) procedures have been proposed in the literature [21, 22]. Evaluating directly stresses at the nodes of each element, or using the stress at the Gauss points, in any case requires then some kind of averaging since stresses are in general different for elements sharing the same node. This averages may incorporate weights based on distances, contributing areas or angles, etc. Other more complicated methods such as 'generalized inversion' [23, 24] work better at interior and exterior nodes, but, due to their computational requirements, can only be performed with regard to part of the mesh. The calculation of the stress state in all the mesh points, for large meshes, may require a computational effort higher than the one needed for the FE analysis itself. Although not among the original objectives of this research, the stress recovery method proposed in this paper seems to satisfy both the requirements of accuracy in the results and simplicity in the procedure.

The content of the paper is structured as follows: in Section 2 the problem of the indetermination of the inter-element forces at corner element nodes is analysed in detail. Then, the definition of inter-element stresses is presented in Section 3. Sections 4 and 5 treats the solution in case of homogeneous and heterogeneous material, respectively. In Section 6, the same method is adapted to mesh boundary nodes with application to stress recovery problem. Section 7 includes examples of the previously treated cases. Finally in Section 8 the main conclusions of the work presented are summarized.

2. INDETERMINATION OF INTER-ELEMENT FORCES

Conventional FE calculations lead to the value of the nodal force $\mathbf{f}$, acting on a generic node, as the sum of the nodal force contributions from each element converging at that node. But, as previously mentioned, the way in which $\mathbf{f}$ splits along the planes of the inter-element interfaces, is a problem that cannot be solved by means of equilibrium equations alone. Considering the example in Figure 2, referring to the inter-element forces as $\mathbf{r}^{(k)}$, and to the nodal forces at node k as $\mathbf{f}^{(k)}$, the equilibrium equations at each node as can be written as in vector

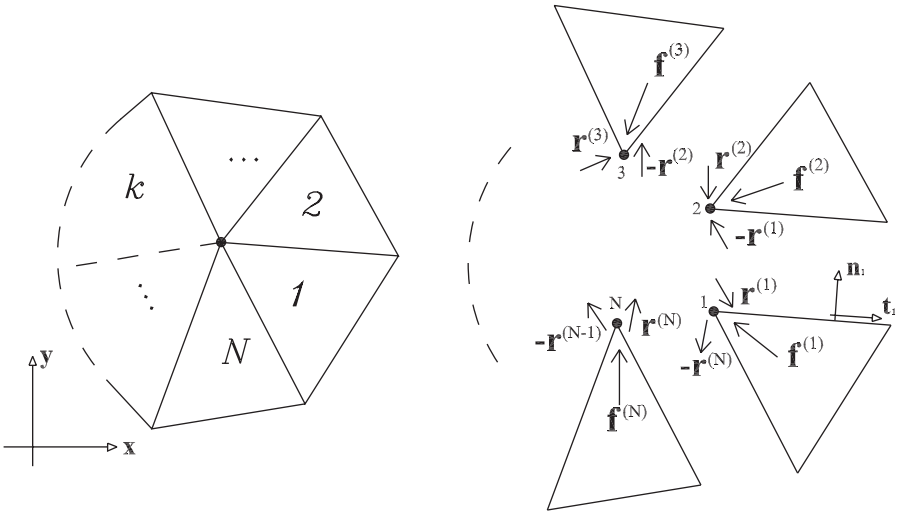

Figure 2. Equilibrated nodal (**f**) and inter-element (**r**) forces at an interior node in a homogeneous medium.

notation as

$$\begin{cases} \mathbf{f}^{(1)} - \mathbf{r}^{(N)} + \mathbf{r}^{(1)} = \mathbf{0} \\ \mathbf{f}^{(2)} - \mathbf{r}^{(1)} + \mathbf{r}^{(2)} = \mathbf{0} \\ \mathbf{f}^{(3)} - \mathbf{r}^{(2)} + \mathbf{r}^{(3)} = \mathbf{0} \\ \vdots \\ \mathbf{f}^{(N)} - \mathbf{r}^{(N-1)} + \mathbf{r}^{(N)} = \mathbf{0} \end{cases} \tag{2}$$

In a 2D context, system (2) appears to have $2N$ equations and $2N$ unknowns ($\mathbf{r}^{(k)}, k = 1, N$), but it is immediate to show that the $2N$ equations in (2) are not independent. In fact, one has N unknown vectorial variables (the inter-element forces $\mathbf{r}^{(k)}$) and $N-1$ independent vectorial equations. This is because nodal forces $\mathbf{f}^{(1)}, \mathbf{f}^{(2)} \ldots \mathbf{f}^{(N)}$ converging at the point must be in equilibrium, i.e. $\sum_{k=1}^{N} \mathbf{f}^{(k)} = \mathbf{0}$; this equation combined with the $N-1$ equations of system (2) leads to the Nth equation in the system. Therefore, having $2N$ unknowns and $2(N-1)$ equations, the system of inter-element forces $\mathbf{r}^{(k)}$ remains undetermined unless two additional equations are added to the system.

3. INTER-ELEMENT STRESSES

Alternatively, one could state that system (2) has two arbitrary variables (in 2D). This argument is actually useful for the developments in the paper. Choosing $\mathbf{r}^{(1)}$ as the arbitrary 2-component

vector and assuming a known value $\bar{\mathbf{r}}$, the remaining unknowns from system (2) can be written as

$$\begin{cases} \mathbf{r}^{(2)} = \bar{\mathbf{r}} - \mathbf{f}^{(2)} \\ \mathbf{r}^{(3)} = \bar{\mathbf{r}} - \mathbf{f}^{(3)} - \mathbf{f}^{(2)} \\ \vdots \\ \mathbf{r}^{(N)} = \bar{\mathbf{r}} - \mathbf{f}^{(N)} - \mathbf{f}^{(N-1)} - \cdots - \mathbf{f}^{(2)} \end{cases} \tag{3}$$

In expanded form, each equation becomes

$$\begin{pmatrix} r_x^{(k)} \\ r_y^{(k)} \end{pmatrix} = \begin{pmatrix} \bar{r}_x \\ \bar{r}_y \end{pmatrix} - \begin{pmatrix} h_x^{(k)} \\ h_y^{(k)} \end{pmatrix} \quad \text{with } k = 1, N \tag{4}$$

being

$$\begin{pmatrix} h_x^{(k)} \\ h_y^{(k)} \end{pmatrix} = \sum_{i=2}^{k} \begin{pmatrix} f_x^{(i)} \\ f_y^{(i)} \end{pmatrix} \quad \text{and} \quad \begin{pmatrix} h_x^{(1)} \\ h_y^{(1)} \end{pmatrix} = \begin{pmatrix} 0 \\ 0 \end{pmatrix} \tag{5}$$

The method developed in the following consists of adding equations to obtain the arbitrary variable $\bar{\mathbf{r}}$, and therefore the rest of inter-element forces $\mathbf{r}^{(k)}$ from system (3).

Inter-element stress is defined as the stress that acts along the surface (or line in 2D) shared by two elements. It is related to the inter-element forces using the simple concept of contributing area. The inter-element forces are spread over the contributing area, leading to a constant stress distribution. These areas can be determined using the principle of virtual work in a way similar to the standard procedure to calculate nodal forces equivalent to external distributed forces. Thus, for linear functions (two-node edge), the nodal area is equal to half of the total surface of the interface; for quadratic functions (three-node edge) and equally spaced nodes on a straight element side, the nodal area associated to a vertex node is equal to a sixth of the total surface, while to a mid-point node, it is equal to two-thirds of the total interface area.

Being $\boldsymbol{n}^{(k)}$ and $\boldsymbol{t}^{(k)}$ the local reference system in the kth plane (Figure 2) (orientation following Mohr's convention), $\Omega^{(k)}$ the element side relative area computed as explained before and $\mathbf{r}^{(k)} = (r_x^{(k)}, r_y^{(k)})$ the inter-element force on the surface in x and y components, the stress traction vector can be written as

$$\boldsymbol{\tau}^{(k)} = \begin{pmatrix} \sigma^{(k)} \\ \tau^{(k)} \end{pmatrix} = \frac{1}{\Omega^{(k)}} \mathbf{Q}^{(k)} \begin{pmatrix} r_x^{(k)} \\ r_y^{(k)} \end{pmatrix} \tag{6}$$

where $\mathbf{Q}^{(k)}$ is the rotation matrix from the global $(\mathbf{x}, \mathbf{y})$ to the local $(\boldsymbol{n}, \boldsymbol{t})$ reference system; the components of the local reference system have been defined as $\boldsymbol{n}^{(k)} = (-\sin\alpha^{(k)}, \cos\alpha^{(k)})$ and $\boldsymbol{t}^{(k)} = (\cos\alpha^{(k)}, \sin\alpha^{(k)})$, being $\alpha^{(k)}$ the anticlockwise angle from $\mathbf{x}$ to $\boldsymbol{t}^{(k)}$.

4. MINIMIZATION PROCEDURE FOR HOMOGENEOUS MATERIAL

Looking at Figure 2, under the assumption of homogeneous and intact material, the existence of a unique stress tensor is verified. If one fixes *a priori* the value of the arbitrary parameter $\bar{\mathbf{r}}$, substituting Equation (4) in Equation (6), the value of the traction vector $\boldsymbol{\tau}^{(k)}$ for each plane k can be computed as a function of $\bar{\mathbf{r}}$ (i.e. $\boldsymbol{\tau}^{(k)} = \boldsymbol{\tau}^{(k)}\{\bar{\mathbf{r}}\}$, where the curly brackets enclose the arguments of a function; this convention is used throughout the paper). Due to the arbitrary value of $\bar{\mathbf{r}}$, the coordinates of $\boldsymbol{\tau}^{(k)}$ on Mohr's space will be representative of points that in general do not belong to any single circle. Denoting with $\mathbf{T}$ the stress tensor at node A, the distance of each point $\boldsymbol{\tau}^{(k)} = (\sigma^{(k)}, \tau^{(k)})$ to the circle representing the tensor $\mathbf{T}$, is the measure of the intrinsic error in the arbitrary choice of $\bar{\mathbf{r}}$. This error is calculated as the distance between the stress vector $\boldsymbol{\tau}^{(k)}\{\bar{\mathbf{r}}\}$ and the projection of $\mathbf{T}$ onto plane k. Borrowing concepts from microplane model [20], a global measure for that error may be expressed as

$$\Phi = \sum_{k=1}^{N} [(\sigma^{(k)}\{\bar{\mathbf{r}}\} - \boldsymbol{n}^{(k)}\mathbf{T}\boldsymbol{n}^{(k)})^2 + (\tau^{(k)}\{\bar{\mathbf{r}}\} - \boldsymbol{t}^{(k)}\mathbf{T}\boldsymbol{n}^{(k)})^2] \tag{7}$$

in which $\boldsymbol{n}^{(k)}\mathbf{T}\boldsymbol{n}^{(k)}$ and $\boldsymbol{t}^{(k)}\mathbf{T}\boldsymbol{n}^{(k)}$ represent the normal and shear components of the projection vector of $\mathbf{T}$ on plane k, and $\sigma^{(k)}$ and $\tau^{(k)}$ are the normal and tangential components of the traction vector $\boldsymbol{\tau}^{(k)}$. One physical interpretation of Φ is represented in Figure 3.

In Equation (7) the only unknown variables are the components of the stress tensor $\mathbf{T}$, if the value of $\bar{\mathbf{r}}$ is assumed unknown. The minimization of Φ with respect to $\mathbf{T}$, (i.e. $\partial\Phi/\partial\sigma_{ij} = 0$), leads to the following system (in matrix notation):

$$\mathbf{A}\boldsymbol{\sigma} = \mathbf{c} \tag{8}$$

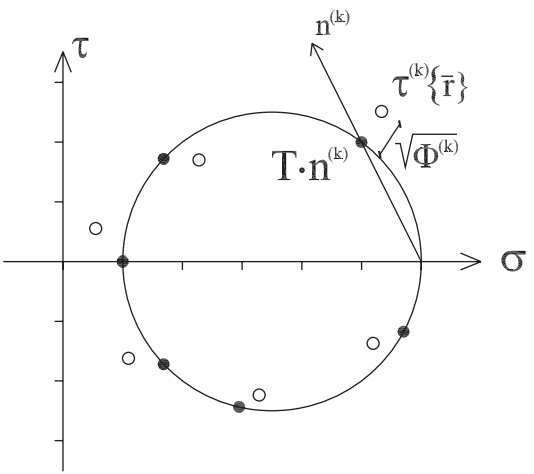

Figure 3. Physical interpretation of the error Φ, as sum of the distances between the traction vector $\boldsymbol{\tau}^{(k)}\{\bar{\mathbf{r}}\}$ and the projection of the stress tensor $\mathbf{T}$ on the plane k whose normal vector is $\mathbf{n}^{(k)}$, for $k = 1, N$.

where

$$\mathbf{A}=\sum_{k=1}^{N}\begin{pmatrix}\sin^2\alpha^{(k)} & -\cos\alpha^{(k)}\sin\alpha^{(k)} & 0\\ -\cos\alpha^{(k)}\sin\alpha^{(k)} & 1 & -\cos\alpha^{(k)}\sin\alpha^{(k)}\\ 0 & -\cos\alpha^{(k)}\sin\alpha^{(k)} & \cos^2\alpha^{(k)}\end{pmatrix} \tag{9}$$

$$\boldsymbol{\sigma}=\begin{pmatrix}\sigma_x\\ \sigma_y\\ \tau_{xy}\end{pmatrix} \quad \text{and} \quad \mathbf{c}=\sum_{k=1}^{N}\begin{pmatrix}\sin^2\alpha^{(k)}\sigma^{(k)}-\cos\alpha^{(k)}\sin\alpha^{(k)}\tau^{(k)}\\ -2\sin\alpha^{(k)}\cos\alpha^{(k)}\sigma^{(k)}-(\sin^2\alpha^{(k)}-\cos^2\alpha^{(k)})\tau^{(k)}\\ \cos^2\alpha^{(k)}\sigma^{(k)}+\cos\alpha^{(k)}\sin\alpha^{(k)}\tau^{(k)}\end{pmatrix} \tag{10}$$

From (8), the stress tensor $\mathbf{T}\{\bar{\mathbf{r}}\}$ that best fits the distribution of $\boldsymbol{\tau}^{(k)}, k=1, N$, is obtained as a function of the arbitrary value of $\bar{\mathbf{r}}$. Now, setting free $\bar{\mathbf{r}}$, i.e. considering it as an unknown variable, if one substitutes $\mathbf{T}\{\bar{\mathbf{r}}\}$ in Equation (7) and minimizes again, this time with respect to $\bar{\mathbf{r}}$, (i.e. $\partial\Phi/\partial\bar{r}_x=0$ and $\partial\Phi/\partial\bar{r}_y=0$), finally the following system is obtained:

$$\begin{pmatrix}D_{11} & D_{12}\\ D_{21} & D_{22}\end{pmatrix}\begin{pmatrix}\bar{\mathbf{r}}_x\\ \bar{\mathbf{r}}_y\end{pmatrix}=\begin{pmatrix}d_1\\ d_2\end{pmatrix} \tag{11}$$

in which matrix $\mathbf{D}$ (symmetric) depends on the geometrical data, while vector $\mathbf{d}$ depends on the mechanical data, that is the input forces $\mathbf{f}^{(k)}$ previously computed through the FE analysis. It is easy to show that the solution of system (11) exists and it is unique.

Matrix $\mathbf{D}$ and vector $\mathbf{d}$ have the following expressions:

$$\mathbf{D}=\mathbf{B}-\mathbf{L}^{\mathrm{T}}\mathbf{A}^{-1}\mathbf{L} \tag{12}$$

$$\mathbf{d}=\mathbf{b}-\mathbf{L}^{\mathrm{T}}\mathbf{A}^{-1}\mathbf{e} \tag{13}$$

being

$$\mathbf{B}=\sum_{k=1}^{N}\begin{pmatrix}\Omega^{(k)^{-2}} & 0\\ 0 & \Omega^{(k)^{-2}}\end{pmatrix} \tag{14}$$

$$\mathbf{L}=\sum_{k=1}^{N}\frac{1}{\Omega^{(k)}}\begin{pmatrix}-\sin\alpha^{(k)} & 0\\ \cos\alpha^{(k)} & -\sin\alpha^{(k)}\\ 0 & \cos\alpha^{(k)}\end{pmatrix} \tag{15}$$

$$\mathbf{b}=\sum_{k=1}^{N}\Omega^{(k)^{-2}}\begin{pmatrix}h_x^{(k)}\\ h_y^{(k)}\end{pmatrix} \tag{16}$$

$$\mathbf{e}=\sum_{k=1}^{N}\frac{1}{\Omega^{(k)}}\begin{pmatrix}-\sin\alpha^{(k)} & 0\\ \cos\alpha^{(k)} & -\sin\alpha^{(k)}\\ 0 & \cos\alpha^{(k)}\end{pmatrix}\begin{pmatrix}h_x^{(k)}\\ h_y^{(k)}\end{pmatrix} \tag{17}$$

Once $\bar{\mathbf{r}}$ is obtained from Equation (11), the inter-element forces can be computed from (3), then the inter-element tractions from (6), and eventually the stress tensor $\mathbf{T}$ from (8).

5. DOUBLE MINIMIZATION PROCEDURE FOR A BI-MATERIAL INTERFACE POINT

On the left-hand side of Figure 4, a set of finite elements converging to node A in a non-homogeneous material is represented. On the right-hand side of the figure the elements are separated and the inter-element forces are reported.

Following intuitive understanding, it is assumed that two different stress tensors exist at that point, one for each material. The stress situation at both sides of the bi-material interface is the one presented in Figure 5, in which two elementary cubes of different materials are presented. Across the interface, equilibrium conditions ensure the identity of the traction vectors on both surfaces. Along the other directions, stress tractions may differ, as shown in the figure. The non-homogeneity, therefore, implies the existence of two different Mohr's circles, one for each material.

In the reference system $(\boldsymbol{n}, \boldsymbol{t})$ of Figure 4 (normal and tangential vector of the bi-material interface), the stress tensors $\mathbf{T}_1$ and $\mathbf{T}_2$ in A, respectively, of material 1 and 2, can be written as follows:

$$\mathbf{T}_1 = \begin{pmatrix} \sigma_0 & \tau \\ \tau & \sigma_1 \end{pmatrix} \quad \text{and} \quad \mathbf{T}_2 = \begin{pmatrix} \sigma_0 & \tau \\ \tau & \sigma_2 \end{pmatrix} \tag{18}$$

The minimization procedure is quite similar to the one presented in the homogeneous case. Equations (3) and (6) are still valid. If the number of elements of material 1 converging at point A is N_1, and the number of elements of material 2 is N_2, the error function Φ may be

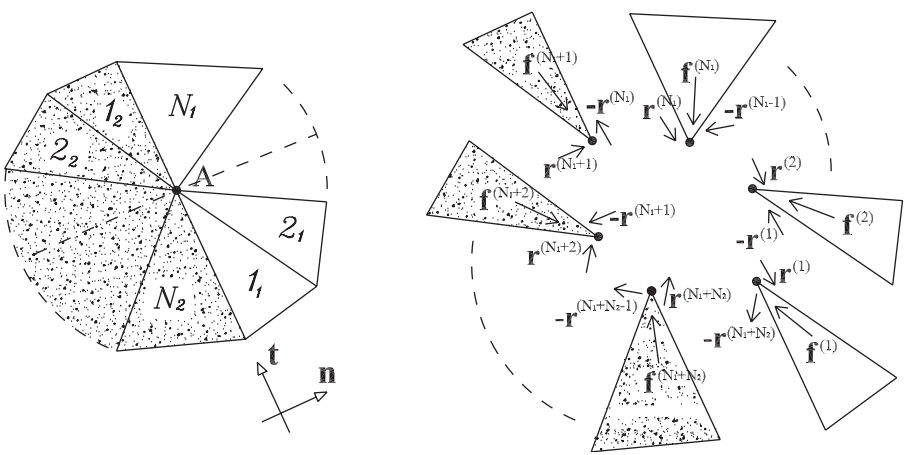

Figure 4. Equilibrated nodal (**f**) and inter-element (**r**) forces in a non-homogeneous medium.

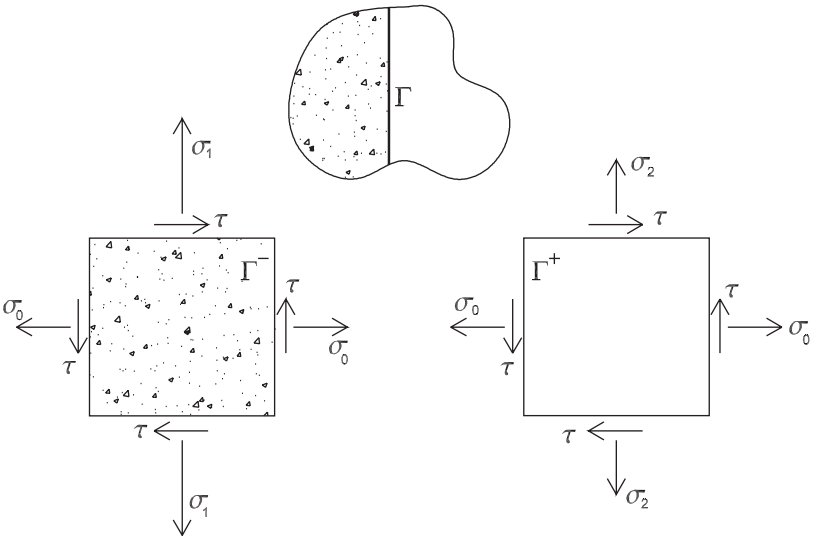

Figure 5. Stress situation involving two continuous elementary cubes at a bi-material interface Γ.

written in this case as $\Phi = \Phi_1 + \Phi_2$, being

$$\begin{aligned}\Phi_1 &= \sum_{k=1}^{N_1} ((\sigma_1^{(k)}\{\bar{\mathbf{r}}\} - \boldsymbol{n}^{(k)}\mathbf{T}_1\boldsymbol{n}^{(k)})^2 + (\tau_1^{(k)}\{\bar{\mathbf{r}}\} - \boldsymbol{t}^{(k)}\mathbf{T}_1\boldsymbol{n}^{(k)})^2) \\ \Phi_2 &= \sum_{k=1}^{N_2} ((\sigma_2^{(k)}\{\bar{\mathbf{r}}\} - \boldsymbol{n}^{(k)}\mathbf{T}_2\boldsymbol{n}^{(k)})^2 + (\tau_2^{(k)}\{\bar{\mathbf{r}}\} - \boldsymbol{t}^{(k)}\mathbf{T}_2\boldsymbol{n}^{(k)})^2)\end{aligned} \tag{19}$$

In the previous expression, the stress vector components, on the kth plane, are $(\sigma_i^{(k)}, \tau_i^{(k)})$, being i the reference to the material.

The unknown variables of Equation (18) are the components of the stress tensor $\mathbf{T}_1$ and $\mathbf{T}_2$, and the arbitrary variable $\bar{\mathbf{r}}$. Following a procedure similar to the one adopted for the homogeneous material, the minimization of Φ with respect to $\mathbf{T}_1$ and $\mathbf{T}_2$, (i.e. $\partial\Phi/\partial\sigma_0 = \partial\Phi/\partial\sigma_1 = \partial\Phi/\partial\sigma_2 = \partial\Phi/\partial\tau = 0$), leads to the system

$$\mathbf{A}\boldsymbol{\sigma} = \mathbf{c} \tag{20}$$

being $\mathbf{A} = \mathbf{A}_1 + \mathbf{A}_2$, where

$$\mathbf{A}_1 = \sum_{k=1}^{N_1} \begin{pmatrix} \sin^2\alpha_1^{(k)} & 0 & 0 & -\cos\alpha_1^{(k)}\sin\alpha_1^{(k)} \\ 0 & \cos^2\alpha_1^{(k)} & 0 & -\cos\alpha_1^{(k)}\sin\alpha_1^{(k)} \\ 0 & 0 & 0 & 0 \\ -\cos\alpha_1^{(k)}\sin\alpha_1^{(k)} & -\cos\alpha_1^{(k)}\sin\alpha_1^{(k)} & 0 & (\sin^2\alpha_1^{(k)} + \cos^2\alpha_1^{(k)})^2 \end{pmatrix} \tag{21}$$

and

$$\mathbf{A}_2 = \sum_{k=1}^{N_2} \begin{pmatrix} \sin^2 \alpha_2^{(k)} & 0 & 0 & -\cos \alpha_2^{(k)} \sin \alpha_2^{(k)} \\ 0 & 0 & 0 & 0 \\ 0 & 0 & \cos^2 \alpha_2^{(k)} & -\cos \alpha_2^{(k)} \sin \alpha_2^{(k)} \\ -\cos \alpha_2^{(k)} \sin \alpha_2^{(k)} & 0 & -\cos \alpha_2^{(k)} \sin \alpha_2^{(k)} & (\sin^2 \alpha_2^{(k)} + \cos^2 \alpha_2^{(k)})^2 \end{pmatrix} \tag{22}$$

and being

$$\boldsymbol{\sigma} = \begin{pmatrix} \sigma_0 \\ \sigma_1 \\ \sigma_2 \\ \tau \end{pmatrix} \quad \text{and} \quad \mathbf{c} = \mathbf{c}_1 + \mathbf{c}_2 \tag{23}$$

with

$$\mathbf{c}_1 = \sum_{k=1}^{N_1} \begin{pmatrix} \sin^2 \alpha_1^{(k)} \sigma_1^{(k)} - \cos \alpha_1^{(k)} \sin \alpha_1^{(k)} \tau_1^{(k)} \\ \cos^2 \alpha_1^{(k)} \sigma_1^{(k)} + \cos \alpha_1^{(k)} \sin \alpha_1^{(k)} \tau_1^{(k)} \\ 0 \\ -2 \sin \alpha_1^{(k)} \cos \alpha_1^{(k)} \sigma_1^{(k)} - (\sin^2 \alpha_1^{(k)} - \cos^2 \alpha_1^{(k)}) \tau_1^{(k)} \end{pmatrix} \tag{24}$$

and

$$\mathbf{c}_2 = \sum_{k=1}^{N_2} \begin{pmatrix} \sin^2 \alpha_2^{(k)} \sigma_2^{(k)} - \cos \alpha_2^{(k)} \sin \alpha_2^{(k)} \tau_2^{(k)} \\ 0 \\ \cos^2 \alpha_2^{(k)} \sigma_2^{(k)} + \cos \alpha_2^{(k)} \sin \alpha_2^{(k)} \tau_2^{(k)} \\ -2 \sin \alpha_2^{(k)} \cos \alpha_2^{(k)} \sigma_2^{(k)} - (\sin^2 \alpha_2^{(k)} - \cos^2 \alpha_2^{(k)}) \tau_2^{(k)} \end{pmatrix} \tag{25}$$

From this point, on the procedure is analogous to the one followed in the homogeneous case. The values of the stress tensor components, computed through Equation (20), are substituted in the expression of Φ. Then, the stress vector components $\sigma_i^{(k)}$ and $\tau_i^{(k)}$ are written as a function of $\bar{\mathbf{r}}$ as in Equation (6). The minimization of Φ with respect to $\bar{\mathbf{r}}$ leads to a system similar to the one presented in Equation (11), whose coefficient matrix and known term vector are presented as follows

$$\mathbf{D} = (\mathbf{B}_1 + \mathbf{B}_2) - (\mathbf{L}_1 + \mathbf{L}_2)^{\mathrm{T}} \mathbf{A}^{-1} (\mathbf{L}_1 + \mathbf{L}_2) \tag{26}$$

$$\mathbf{d} = (\mathbf{b}_1 + \mathbf{b}_2) - (\mathbf{L}_1 + \mathbf{L}_2)^{\mathrm{T}} \mathbf{A}^{-1} (\mathbf{e}_1 + \mathbf{e}_2) \tag{27}$$

being

$$\mathbf{B}_1 = \sum_{k=1}^{N_1} \begin{pmatrix} \Omega_1^{(k)^{-2}} & 0 \\ 0 & \Omega_1^{(k)^{-2}} \end{pmatrix} \quad \text{and} \quad \mathbf{B}_2 = \sum_{k=1}^{N_2} \begin{pmatrix} \Omega_2^{(k)^{-2}} & 0 \\ 0 & \Omega_2^{(k)^{-2}} \end{pmatrix} \tag{28}$$

$$\mathbf{L}_1 = \sum_{k=1}^{N_1} \frac{1}{\Omega_1^{(k)}} \begin{pmatrix} -\sin\alpha_1^{(k)} & 0 \\ 0 & \cos\alpha_1^{(k)} \\ 0 & 0 \\ \cos\alpha_1^{(k)} & -\sin\alpha_1^{(k)} \end{pmatrix} \quad \text{and} \quad \mathbf{L}_2 = \sum_{k=1}^{N_2} \frac{1}{\Omega_2^{(k)}} \begin{pmatrix} -\sin\alpha_2^{(k)} & 0 \\ 0 & 0 \\ 0 & \cos\alpha_2^{(k)} \\ \cos\alpha_2^{(k)} & -\sin\alpha_2^{(k)} \end{pmatrix} \tag{29}$$

$$\mathbf{b}_1 = \sum_{k=1}^{N_1} \Omega_1^{(k)^{-2}} \begin{pmatrix} h_{1x}^{(k)} \\ h_{1y}^{(k)} \end{pmatrix} \quad \text{and} \quad \mathbf{b}_2 = \sum_{k=1}^{N_2} \Omega_2^{(k)^{-2}} \begin{pmatrix} h_{2x}^{(k)} \\ h_{2y}^{(k)} \end{pmatrix} \tag{30}$$

$$\mathbf{e}_1 = \sum_{k=1}^{N_1} \frac{1}{\Omega_1^{(k)}} \begin{pmatrix} -\sin\alpha_1^{(k)} & 0 \\ 0 & \cos\alpha_1^{(k)} \\ 0 & 0 \\ \cos\alpha_1^{(k)} & -\sin\alpha_1^{(k)} \end{pmatrix} \begin{pmatrix} h_{1x}^{(k)} \\ h_{1y}^{(k)} \end{pmatrix} \tag{31}$$

and

$$\mathbf{e}_2 = \sum_{k=1}^{N_2} \frac{1}{\Omega_2^{(k)}} \begin{pmatrix} -\sin\alpha_2^{(k)} & 0 \\ 0 & 0 \\ 0 & \cos\alpha_2^{(k)} \\ \cos\alpha_2^{(k)} & -\sin\alpha_2^{(k)} \end{pmatrix} \begin{pmatrix} h_{2x}^{(k)} \\ h_{2y}^{(k)} \end{pmatrix} \tag{32}$$

with the slight difference, this time, between h_1 and h_2:

$$\begin{pmatrix} h_{1x}^{(k)} \\ h_{1y}^{(k)} \end{pmatrix} = \sum_{i=2}^{k} \begin{pmatrix} f_x^{(i)} \\ f_y^{(i)} \end{pmatrix}, \begin{pmatrix} h_{2x}^{(k)} \\ h_{2y}^{(k)} \end{pmatrix} = \sum_{i=2}^{N_1+k} \begin{pmatrix} f_x^{(i)} \\ f_y^{(i)} \end{pmatrix} \quad \text{and} \quad \begin{pmatrix} h_x^{(1)} \\ h_y^{(1)} \end{pmatrix} = \begin{pmatrix} 0 \\ 0 \end{pmatrix} \tag{33}$$

Once $\bar{\mathbf{r}}$ is obtained using Equations (26) and (27), the inter-element forces can be computed by means of nodal equilibrium equations (3), then the inter-element tractions obtained from Equation (6), and finally the components of the stress tensors $\mathbf{T}_1$ and $\mathbf{T}_2$ from (20).

6. NODES AT THE BOUNDARY

For nodes along the mesh boundaries, the indetermination of the inter-element forces does not exist, as shown in the following. Nevertheless, the method of the minimization previously presented is still suitable for computing a stress tensor $\mathbf{T}$ at boundary points.

In Figure 6 an example of a boundary node A and N elements (that is $N-1$ interfaces) is presented. A simplified case, in which the load is acting only along the perpendicular direction of the surface, is considered. Once again, the N equilibrium equations at the N nodes are not

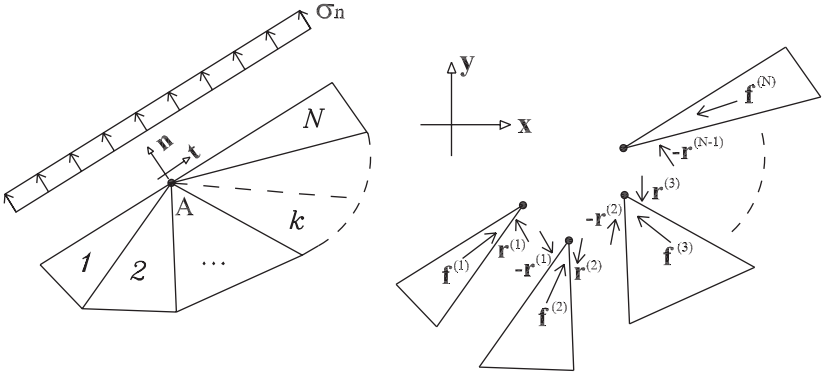

Figure 6. Equilibrated nodal (**f**) and inter-element (**r**) forces at a boundary node.

linearly independent:

$$\begin{cases} \mathbf{f}^{(1)} + \mathbf{r}^{(1)} = 0 \\ \mathbf{f}^{(2)} - \mathbf{r}^{(1)} + \mathbf{r}^{(2)} = 0 \\ \mathbf{f}^{(3)} - \mathbf{r}^{(2)} + \mathbf{r}^{(3)} = 0 \\ \vdots \\ \mathbf{f}^{(N)} - \mathbf{r}^{(N-1)} = 0 \end{cases} \tag{34}$$

but, this time, the inter-element forces $\mathbf{r}^{(k)}$ are $N-1$ and can be computed without indetermination (the last of Equations (34) is redundant) using the first $N-1$ equations in Equations (34):

$$\begin{cases} \mathbf{r}^{(1)} = -\mathbf{f}^{(1)} \\ \mathbf{r}^{(2)} = -\mathbf{f}^{(1)} - \mathbf{f}^{(2)} \\ \mathbf{r}^{(3)} = -\mathbf{f}^{(1)} - \mathbf{f}^{(2)} - \mathbf{f}^{(3)} \\ \vdots \\ \mathbf{r}^{(N-1)} = -\mathbf{f}^{(1)} - \mathbf{f}^{(2)} - \cdots - \mathbf{f}^{(N-1)} \end{cases} \tag{35}$$

or, in expanded notation, as

$$\begin{pmatrix} r_x^{(k)} \\ r_y^{(k)} \end{pmatrix} = \sum_{i=1}^{k} \begin{pmatrix} -f_x^{(i)} \\ -f_y^{(i)} \end{pmatrix} \tag{36}$$

with $k = 1, N-1$.

The stress tensor $\mathbf{T}'$ in A, in the local reference system $(\boldsymbol{n}, \boldsymbol{t})$ components, can be written as

$$\mathbf{T}' = \begin{pmatrix} \sigma_n & \tau_{nt} \\ \tau_{nt} & \sigma_t \end{pmatrix} \tag{37}$$

in which σ_n is the perpendicular distributed known load along the surface, τ_{nt} is equal to zero for the hypothesis before mentioned, and σ_t must be computed.

In the global reference system $(\mathbf{x}, \mathbf{y})$, $\mathbf{T}$ can be expressed, in terms of the components of $\mathbf{T}'$, as

$$\begin{pmatrix} \sigma_x & \tau_{xy} \\ \tau_{xy} & \sigma_y \end{pmatrix} = \begin{pmatrix} \frac{1}{2}[\sigma_n + \sigma_t + (\sigma_t - \sigma_n)\cos 2\beta] & \frac{1}{2}(\sigma_t - \sigma_n)\sin 2\beta \\ \frac{1}{2}(\sigma_t - \sigma_n)\sin 2\beta & \frac{1}{2}[\sigma_n + \sigma_t + (\sigma_n - \sigma_t)\cos 2\beta] \end{pmatrix} \tag{38}$$

with β equal to the anticlockwise angle from $\mathbf{x}$ to $\boldsymbol{t}$.

The inter-element stresses can be obtained by substituting Equation (36) in Equation (6). The stress tensor $\mathbf{T}$ is computed by minimizing the error function (7) with respect to σ_t, (i.e. $\partial\Phi/\partial\sigma_t = 0$); this leads to

$$\sigma_t = \frac{\sum_{k=1}^{N} [\sigma^{(k)} \sin^2(\beta - \alpha^{(k)}) + \tau^{(k)} \cos(\beta - \alpha^{(k)}) \sin(\beta - \alpha^{(k)})]}{\sum_{k=1}^{N} \sin^2(\beta - \alpha^{(k)})} \tag{39}$$

This stress recovery process is a simple alternative way to obtain the stress state at a boundary node.

7. EXAMPLES

In this section, some examples of calculation of inter-element forces, tractions and stress tensor at internal and boundary nodes, are presented. Whenever possible, the results obtained will be compared to theoretical solutions. The stress tensor calculated will also be compared to stress values obtained from a standard smoothing procedure based on the average stress of the nearby Gauss points. Other more refined forms of smoothing could be also considered (e.g. weighted average in terms of angles, distances, etc.). However, stress recovery is not the central object of this paper, but only a by-product of the proposed procedure mainly oriented to computing inter-element forces.

7.1. Uniform stress state in homogeneous material

In Figure 7, a square specimen of 1×1 m dimension, elastic modulus $E = 10^4$ MPa, and Poisson ratio $v = 0.2$, is shown. From (a) to (h) various meshes are considered. All of them are calculated using linear first and then quadratic elements. The influence of the regularity of the discretization and the number of planes converging at the internal node A on the inter-element forces, tractions and stresses at the node, is studied. A hydrostatic and non-hydrostatic, but uniform, stress state has been applied in plane stress, as shown in Figure 7(i). In the case of hydrostatic stresses, the solution obtained by the minimization of Φ has been compared to the prescribed stresses. For all meshes presented in Figure 7 the error of the obtained results is zero (i.e. the stress tensor recovered at node A matched exactly the applied stress-state, and the stress tractions calculated across each line converging at node A, turn out exactly equal to the applied pressure).

Considering the non-hydrostatic stress state in Figure 7(i), the results of the proposed method match exactly the applied stress and corresponding tractions, and as a sample only the solution in terms of inter-element stresses and tractions for mesh (h) is presented in (l). One can see

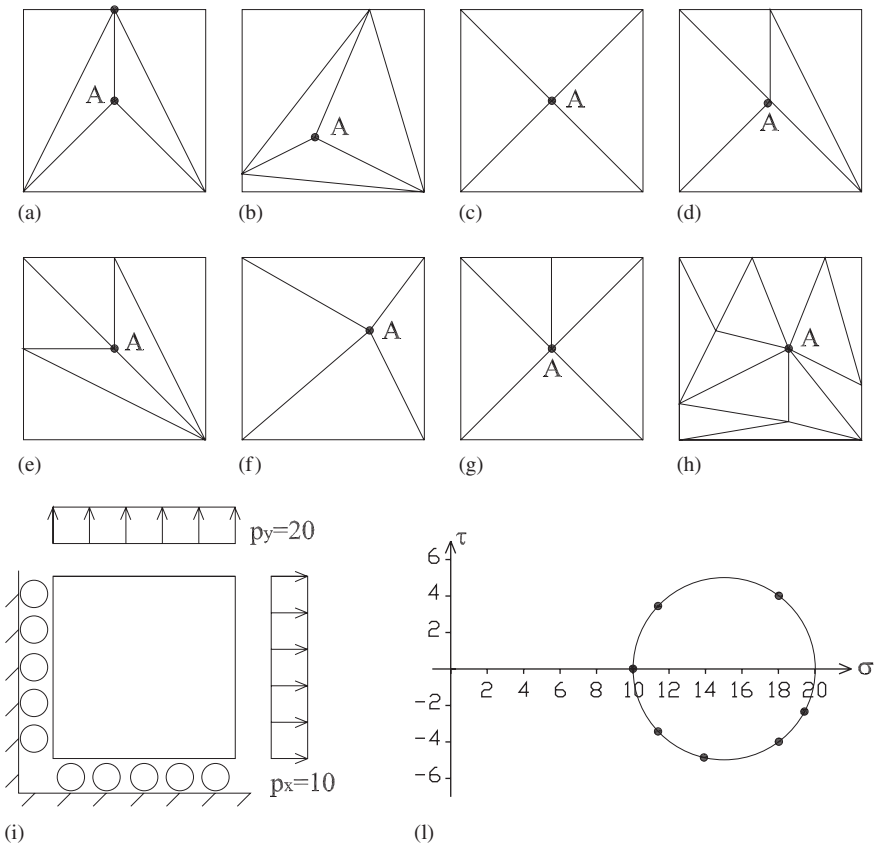

Figure 7. Uniform stress state; meshes used (a)–(h), loading state (i), and results for case h (l).

that the Mohr's circle reproduces exactly the stress condition in A, as well as the dots do for the stress vector in each plane i. The comparison with the smoothing procedure based on the average of the stress values at the Gauss points is omitted. In fact, in case of constant stress state, the linear triangular elements also yield exact solution, and therefore the results of this procedure and classical smoothing coincide.

7.2. Non-uniform stress state in homogeneous material

In this case, the same square specimen of Figure 7 considered before is subjected to gravity load. The simulation is performed in plane strain. The specific mass is $0.1\ \mathrm{Kg_m/m^3}$ and the gravity acceleration considered is $10\ \mathrm{m/s^2}$. In Figure 8, the various meshes considered are depicted from (a) to (c). They are selected to study the influence of the element-density while the number and orientation of the lines converging on node A is maintained. Last mesh (d), on the other hand, represents a case of irregular mesh. Also this time, the analysis has been performed using first linear and then quadratic elements. The stress state at node A and the

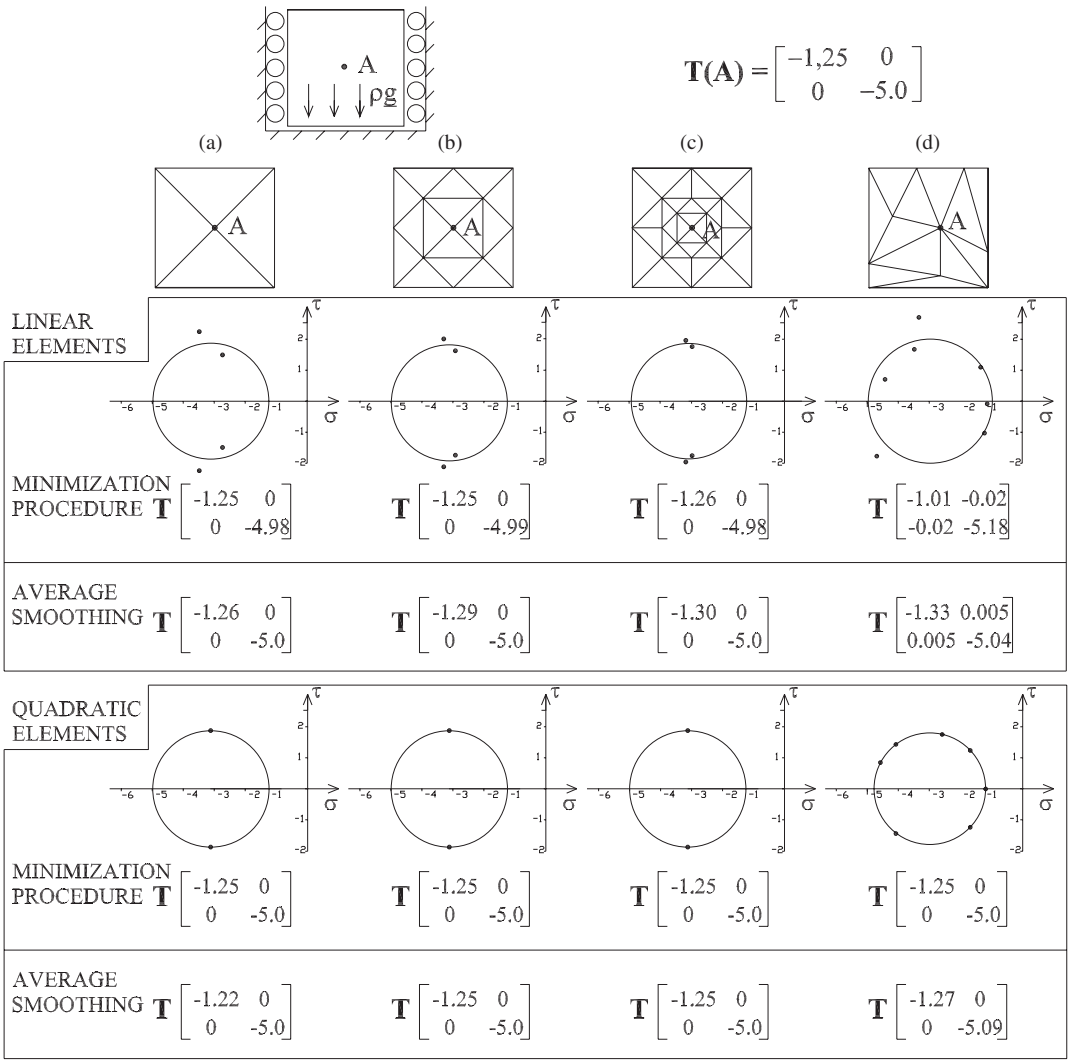

Figure 8. Non-uniform stress state; meshes, loading and results.

tractions along the lines converging at that point, which are obtained with the new procedure and represented in Figure 8, are investigated.

From basic statics it is known that stress state at point A should be given by $\sigma_x = -1.25\,\mathrm{N/m}$, $\sigma_y = -5.0\,\mathrm{N/m}$ and $\tau_{xy} = 0\,\mathrm{N/m}$. Due to the poorness of constant strain triangles, it is also known that the non-uniform stress state cannot be captured exactly and a refinement of the mesh is required in order to represent a staircase-type stress distribution. This is clearly shown in the upper part of Figure 8, for meshes (a)–(c). The results are represented in Mohr's space $\sigma - \tau$, with the circle representing the calculated stress tensor, and the dots the tractions on the concurrent planes at point A. It can be observed in the sequence (a)–(c) for linear

elements, that the finer the mesh, the closer the dots to the circle. This means that the exact solution is approached from (a) to (c). Below each circle, the values of the stress tensor **T** at A, computed through the minimization method as well as through the average smoothing procedure, are reported. It can be observed that, for linear elements, from mesh (a) to (c), both methods give reasonable results, even if the ones observed by the proposed method seem more accurate. The accuracy of the proposed minimization procedure appears more evident for quadratic elements, as shown in the bottom part of Figure 8, since the exact solution is obtained even for the coarsest mesh (a).

From the strict view point of the stress tensor recovery at the nodes ('smoothing'), the advantage of the method presented in this work with respect to the average smoothing procedure may not be evident in the case of regular mesh and linear elements, although the method allows to obtain additionally the value of equilibrated inter-elements forces and stresses across the planes departing from A. For irregular mesh, as the one presented in Figure 8(d); the linear elements return inaccurate results due to the non-uniform stress state. On the other hand, the quadratic elements are able to reproduce the gravity stress state in the specimen. The stress tensor in A is perfectly computed by means of the minimization method, while less precise results are obtained through the average smoothing procedure.

The following example concerns the analysis of the stress state at the interior point A of the beam shown in Figure 9(a). The beam dimensions are $l = 12.0\,\text{m}$, $h = 1.2\,\text{m}$ and the width 1 m. The coordinates of point A are $x_A = 4\,\text{m}$ and $y_A = 0.2\,\text{m}$. A three point bending test has

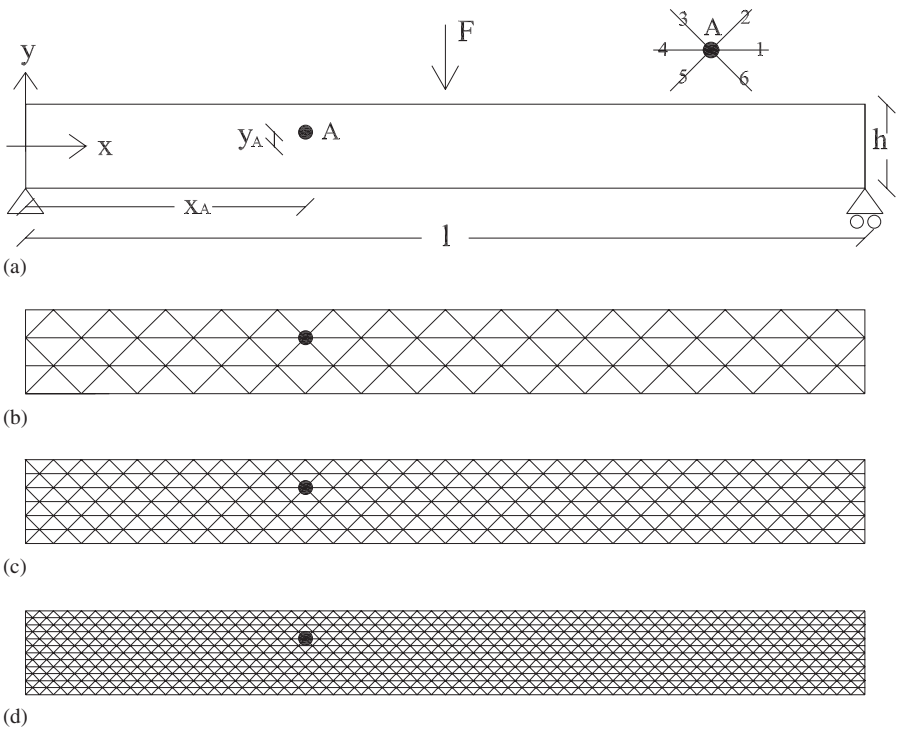

Figure 9. Three-point bending test: (a) geometry of the beam; and (b)–(d) refinement of the mesh.

been performed, using a force F equal to 1000 KN. For the FE analysis three different meshes have been used, as shown in Figure 9(b)–(d). The test has been developed using first linear and then quadratic triangular elements. The coarsest mesh (b) has 93 elements, the middle (c) has 366 elements and the finest (d) 1452.

The stress state at point A obtained from beam theory is

$$\begin{aligned} \sigma_x &= \frac{M_A}{I_z} y_A = 2.77 \ \text{[MPa]} \\ \tau_{xy} &= \alpha_V \frac{V_A}{A} = 0.55 \ \text{[MPa]} \end{aligned} \tag{40}$$

being M_A the bending moment in A, V_A the shear at cross-section including point A, I_z the moment of inertia of the cross-section and α_V the shear factor.

A comparison between values obtained with these formulas and the ones obtained from the FE analysis plus the proposed procedure, as well as from standard average smoothing, is shown in Figure 10 in terms of σ_x and τ_{xy}. In the figure, these values are plotted against the number of elements in logarithmic scale. As previously observed, the results obtained with quadratic elements (the black dots in Figure 10) are exact and they seem not to be affected by the refinement of the mesh, while the ones obtained by linear elements (the crosses in Figure 10) show a tendency to convergence as long as the number of elements increases.

In Figure 11 the stress state in A is presented in terms of Mohr's circles and stress tractions. On the left-hand side of the figure, the circles refer to the analysis with linear elements, on the right-hand side with quadratic elements. Rows (B), (C) and (D) refer to meshes (b), (c) and (d), respectively, in Figure 9. The dots represent the stress state along the planes as numbered on the right-hand side of Figure 9. Using linear elements, the dots are closer to the circle as long as the refinement of the mesh increases (this means that the error estimation of the stress state in A decreases). For quadratic elements, a zero-error result is obtained from the coarsest mesh, since all the dots lie on the circles.

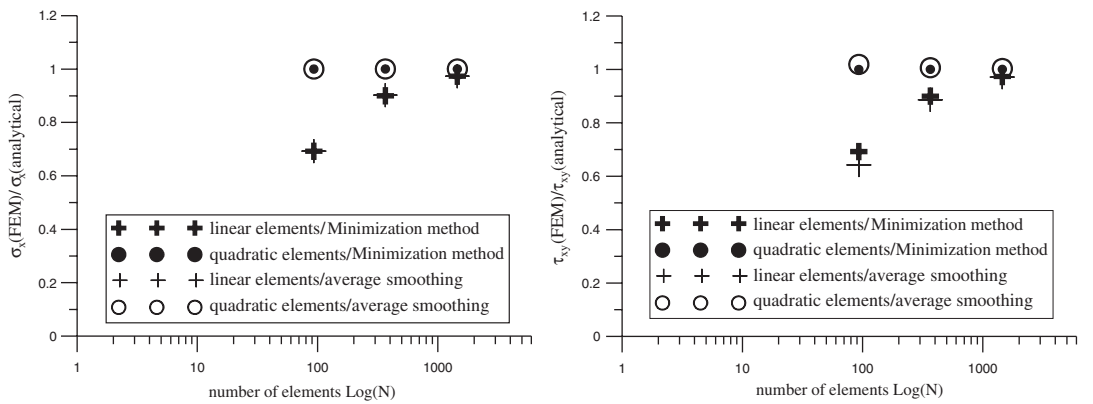

Figure 10. σ_x (on the left) at point A of specimen in Figure 9 and τ_{xy} (on the right) vs number of mesh elements, for linear (crosses) and quadratic (dots) elements using the minimization procedure presented in this paper (**bold** symbols) and a Gauss-point average stress recovery.

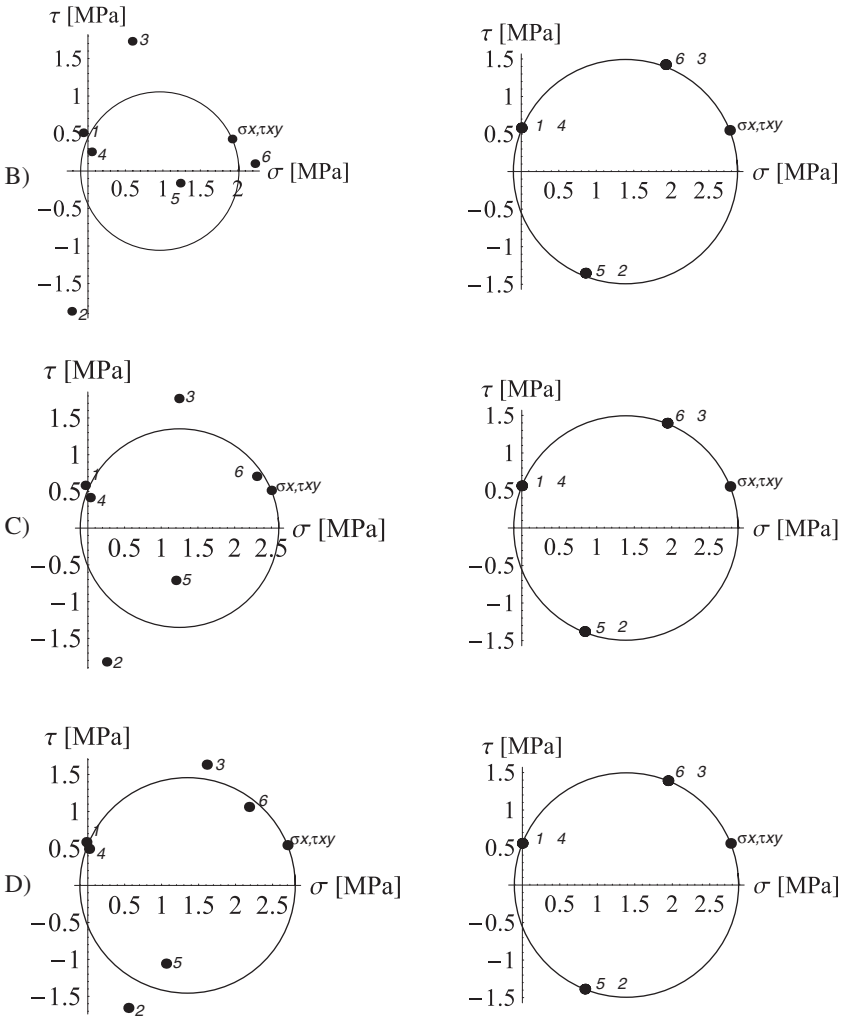

Figure 11. Mohr's circle at point *A* of specimen in Figure 9: on the left, results obtained using linear elements; on the right, results obtained using quadratic elements. (B), (C) and (D) refer to (b), (c) and (d) meshes in Figure 9, respectively.

7.3. Heterogeneous material

The following are some results regarding the case of an heterogeneous material. In Figure 12, a heterogenous composite specimen made of particles embedded in a matrix is represented.

The specimen dimension is 20×20 mm, and the mechanical characteristics used are: $E = 500\,000$ MPa, $v = 0.2$ for the particles (material 1) and $E = 100\,000$ MPa, $v = 0.2$ for the matrix (material 2). The values selected have a pure academic purpose; no specific real material has been simulated. The bottom surface of the specimen is constrained as shown in Figure 12;

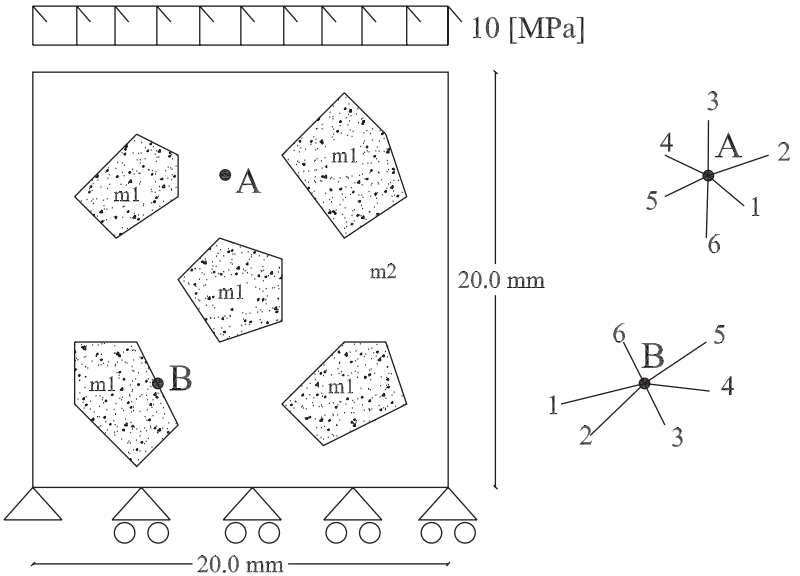

Figure 12. Specimen of a heterogeneous material made by some aggregates (m1) embedded in a matrix (m2); on the right-hand side, the mesh lines departing from nodes A and B.

the upper surface is loaded by normal tensile tractions of 10 MPa. Different mesh refinements have been considered, as shown in Figure 13, always using linear triangular elements and such that the mesh lines concurring at points A and B remain the same in the different levels of refinement (see sketches on the right-hand side of Figure 12).

For node A, the stress state obtained is represented in Figure 14 in terms of Mohr's circles and stress tractions. Since node A is surrounded by a single material, the stress state is represented by only one circle. In Figure 15 the stress components σ_x and σ_y obtained at node A are plotted against the number of elements in the mesh. A clear convergence is shown in the figure.

Node B shows the same stress situation presented in Figure 5, as the stress state is defined by two Mohr's circles. The results in terms of Mohr's circles are shown in Figure 16, and the number assigned to each dot follows the numbering of the planes on the sketch on the right-hand side of Figure 12. The values of the stress components along x and y directions for material 1 and 2 are plotted in Figure 17 against the number of elements in the mesh.

The distance between the dots and the circles represents the error in the minimization procedure. One can appreciate the steadiness of the solution in Figures 15 and 17 which is obtained using this procedure, and the accuracy of solution in Figures 14 and 16, respectively for node A and B.

7.4. Boundary node

In Section 6 it has been shown that for boundary nodes, the inter-element forces can be computed by equilibrium equations alone (no static indetermination), so the method is used

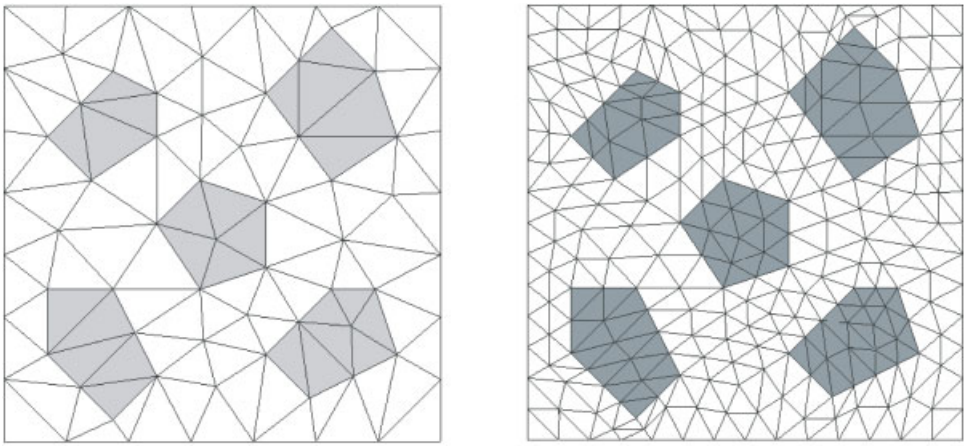

Figure 13. Refinements for the specimen shown in Figure 12; the mesh lines of mesh 1 remain constant in meshes 2, 3 and 4.

only to compute the stress tensor **T**, as a stress recovery technique. This case is illustrated in this section with one example representing a four-point bending test for the beam showed in Figure 18(a). The two forces acting on the beam are of 10 KN each, the length l of the beam is 3 m, the height h equal to 0.3 m, and the width is 1 m.

The test has been performed using different mesh refinements, from the coarsest in Figure 18(b) to the finest in Figure 18(f), first using linear and then quadratic triangular elements. The minimization method is applied for node A, and the results are then compared to the ones obtained by the Gauss point stress average smoothing procedure. In Table I, the FE characteristics of each mesh are reported.

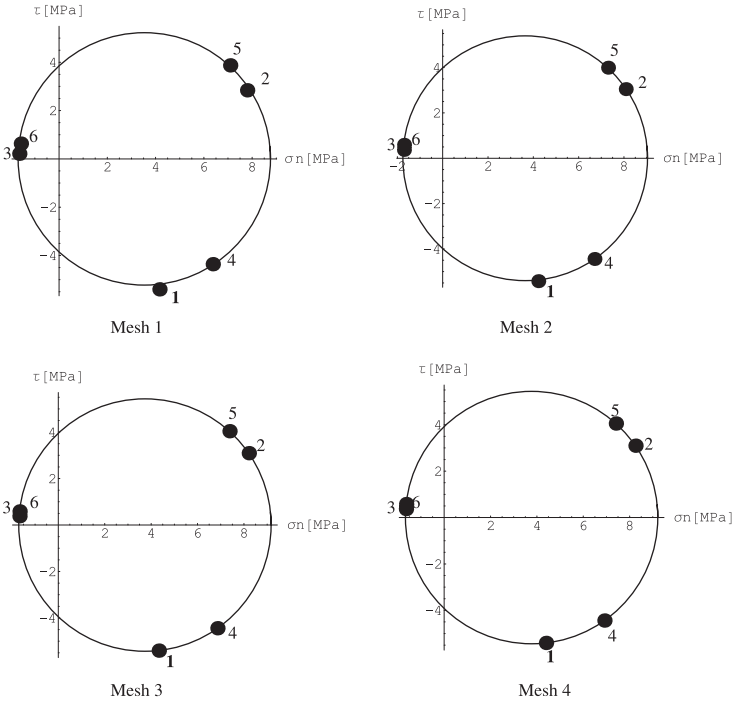

Figure 14. Mohr's circle at node A of specimen in Figure 12 obtained using different meshes as presented in Figure 13. The dots represent the stress tractions along the directions of the mesh lines.

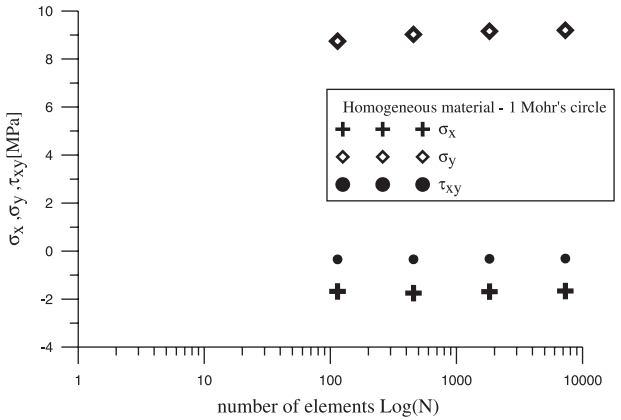

Figure 15. Stress components along x and y directions vs number of elements contained in the mesh, for node A of specimen in Figure 12.

From the beam theory, the maximum stress at the top fibre of the mid-cross section is

$$\sigma_{\max} = \frac{Fe}{I}\,\frac{h}{2} = 20 \ [\text{MPa } 10^{-2}] \tag{41}$$

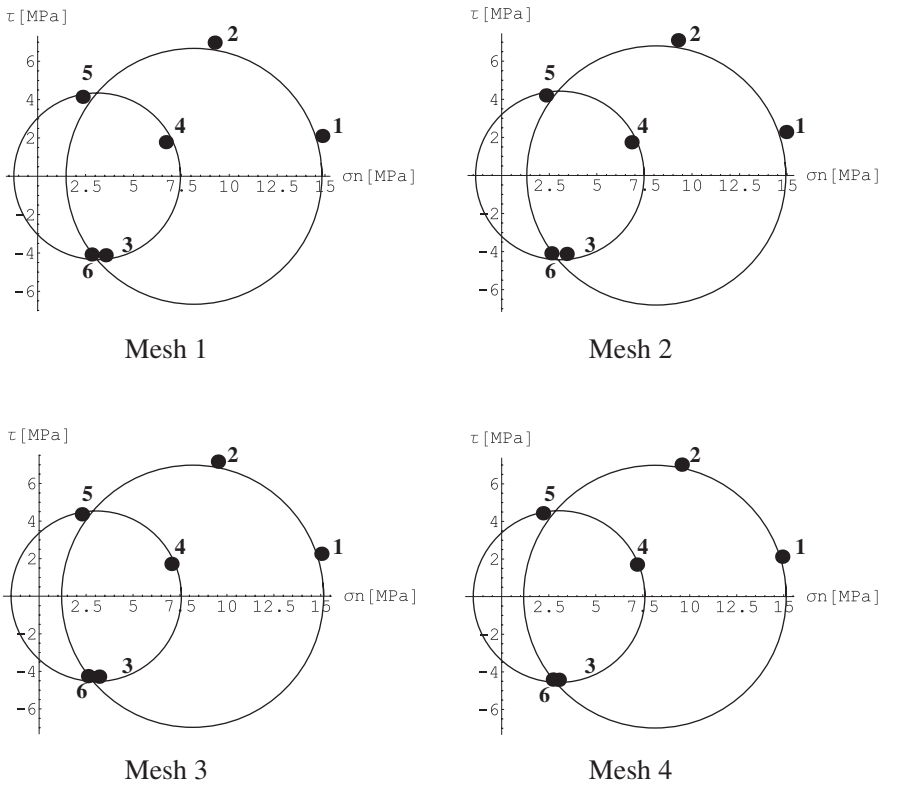

Figure 16. Mohr's circles at node *B* of specimen of Figure 12 obtained using different meshes presented in Figure 13. The two circles represent the stress state in material 1 (particles) and 2 (matrix).

Table I. Element and node number in mesh refinement.

Mesh	# Elements	# Linear nodes	# Quadratic nodes
(b)	40	32	103
(c)	160	103	365
(d)	360	214	787
(e)	1440	787	3013
(f)	5760	3013	11 785

In Figure 19 the maximum compressive stress in the mid-cross-section is reported vs the number of elements for each mesh, in logarithmic scale. The bold crosses and the bold dots represent, respectively, the values obtained with the linear and quadratic analysis and the proposed minimization procedure; in the same graphic, the crosses and the circles are the results from linear and quadratic mesh obtained with the average smoothing procedure.

Both methods show convergence to the theoretical solution, although the proposed procedure converges fasters for both linear and quadratic elements. Actually, the results of the proposed

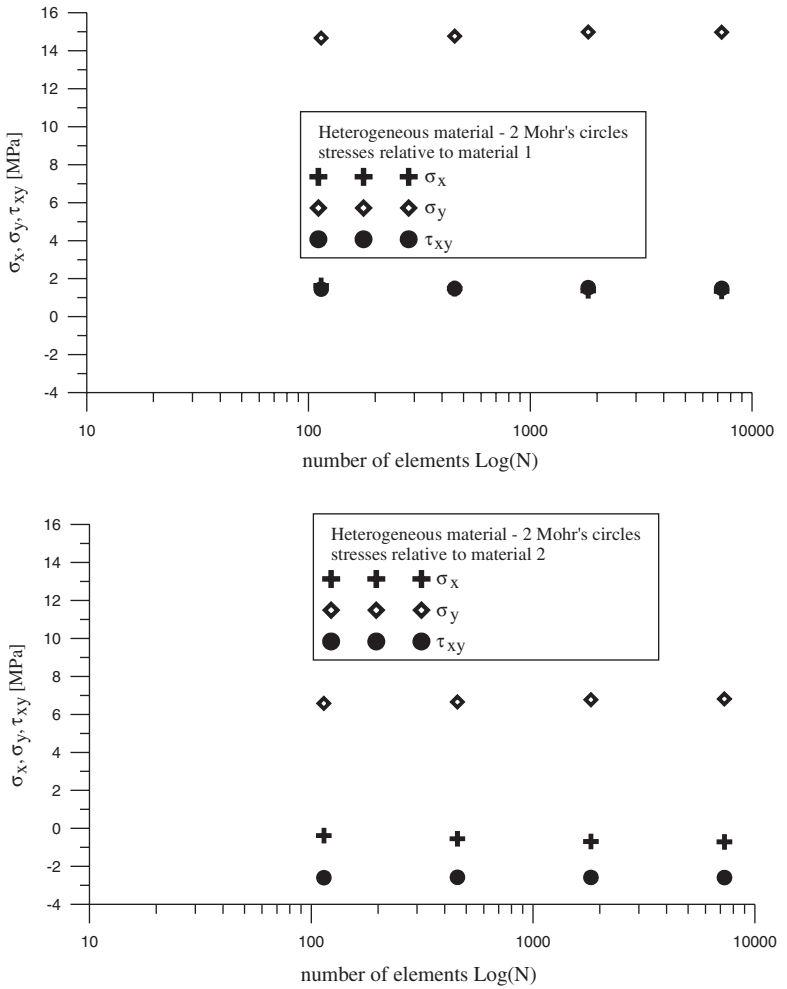

Figure 17. Stress components along x and y directions vs number of elements contained in the mesh, at node B of specimen of Figure 12; at the top the results refer to material 1 (particles), at the bottom they refer to material 2 (matrix).

procedure for the quadratic elements are exact for even the coarsest mesh, while this is not the case for standard Gauss point averaging.

8. SUMMARY AND CONCLUSIONS

The formulation of a minimization procedure for the calculation of inter-element forces and tractions as well as stress state at nodes as a post-processing step in the standard FE-displacement formulation has been presented. Its application to simple and theoretically known cases has been investigated. The method provides, by reproducing an accurate stress state at the nodes,

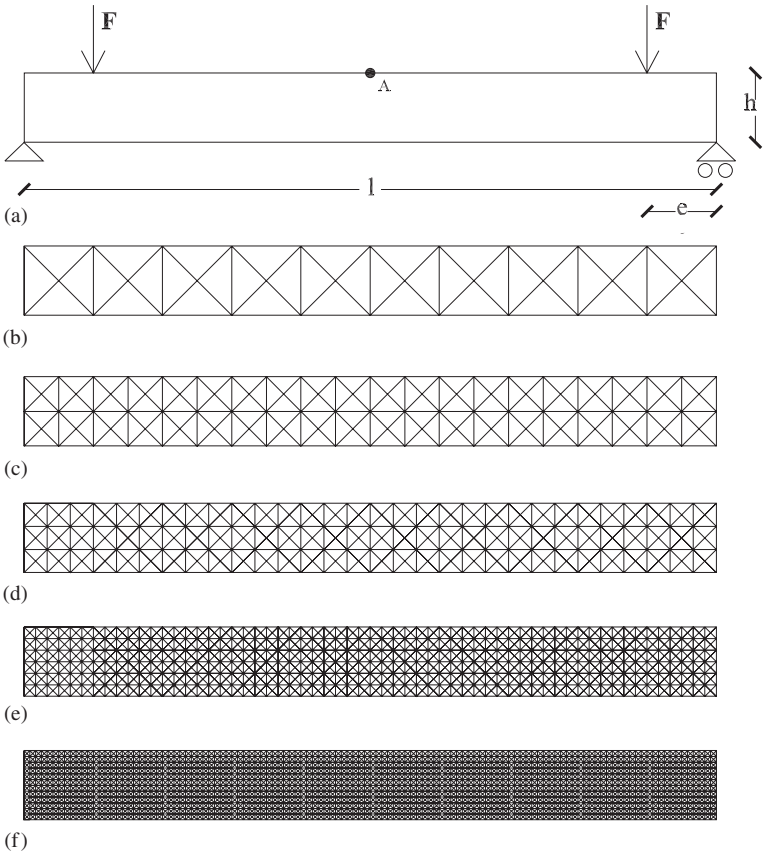

Figure 18. Four-point bending test: (a) geometry of the beam; and from (b) to (f) refinement of the mesh.

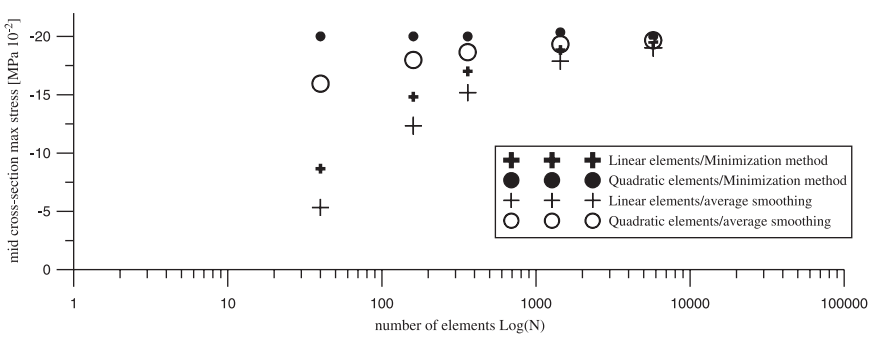

Figure 19. Maximum mid-cross- section stress values at point *A* of the beam presented in Figure 18, obtained using the minimization procedure presented in this paper (**bold** symbols) and compared with the results using an average smoothing method.

a good evaluation of the inter-element forces at element corner nodes. The examples have been developed using linear and quadratic elements, and the stress tensor obtained has been compared to the ones obtained with simple average smoothing procedure. The results show that the method proposed succeeds in producing meaningful equilibrated inter-element forces and tractions at corner element nodes without the need to resort to the traditional double-noded interface elements. Additionally, this method also turns out to be a good way to evaluate the stress state at the nodes, with at least the same accuracy (or clearly higher for the boundary nodes) as the traditional average smoothing procedure. It is easy implementable and it is not affected by the dimension of the mesh. The solving algorithm consists of the inversion of a 2×2 symmetric matrix and a matrix-vector product, to be repeated n times, being n the number of the nodes of the mesh.

ACKNOWLEDGEMENTS

The first author wants to thank MIUR (Rome) for the support received and AGAUR-DURSI (Barcelona) for her fellowships. Research grant MAT2003-02481 from MEC (Madrid) is also gratefully acknowledged.

REFERENCES

1. Ingraffea AR, Saouma VE. Numerical modelling of discrete crack propagation in reinforced and plain concrete. In *Fracture Mechanics of Concrete*, Sih GC, DiTomasso A (eds). Martinus Nijhiff: Dordrecht, The Netherlands, 1985; 171–225.
2. Bittencourt TN, Ingraffea AR, Llorca J. Simulation of arbitrary, cohesive crack propagation. In *Fracture Mechanics of Concrete Structures* (*FRAMCOS1*), Bažant ZP (ed.). Elsevier: Breckenridgr, Colorado, 1992; 171–225.
3. Rots JG. Computational modeling of concrete. *Ph.D. Thesis*, TU Delft, 1988.
4. Belytschko T, Black T. Elastic crack growth in finite elements with minimal remeshing. *International Journal for Numerical Methods in Engineering* 1999; **45**:601–620.
5. Oliver J, Cervera M, Manzoli O. Strong discontinuities and continuum plasticity models: the strong discontinuity approach. *International Journal of Plasticity* 1999; **15**:319–351.
6. Ngo D, Scordelis AC. Finite element analysis of reinforced concrete beams. *Journal of the American Concrete Institute* 1967; **64**(14):152–163.
7. Rots JG, Schellekens JCJ. Interface elements in concrete mechanics. In *Computer-Aided Analysis and Design of Concrete*, Bićanić N, Mang H (eds), vol. 2. Pineridge Press: Zell-am-See, Austria, 1990; 909–918.
8. Camacho GT, Ortiz M. Computational modelling of impact damage in brittle materials. *International Journal of Solids and Structures* 1996; **33**(20–22):2899–2938.
9. Lopez CM, Carol I. Numerical analysis of concrete microstructure using interface elements. *Anales de Mecanica de la Fractura* 1995; **12**:75–80.
10. Carol I, Lopez CM, Roa O. Micromechanical analysis of quasi-brittle materials using fracture-based interface elements. *International Journal for Numerical Methods in Engineering* 2001; **52**(1/2):193–215.
11. Sluys LJ, Berends AH. 2D/3D modelling of crack propagation with embedded discontinuity elements. *Computational Modelling of Concrete Structures (EURO-C)*, Badgastein, Austria, 1998; 399–408.
12. Gens A, Carol I, Alonso E. An interface element formulation for the analysis of soil-reinforcement interaction. *Computers and Geotechnics* 1988; **7**:133–151.
13. Lopez CM, Carol I, Aguado A. Fracture of microstructural concrete: a numerical study using interface elements. In *Contemporary Research in Engineering Science*, *Proceedings of Eringen Medal Symposium Honoring S.N. Atluri*, Batra R (ed). Springer: New Orleans, 1995; 327–328.
14. Ciancio D, Lopez CM, Carol I, Cuomo M. New results in meso-mechanical modelling of concrete using fracture-based zero-thickness interface elements. *Computational Modelling of Concrete Structures (EURO-C)*, Sankt Johann, Austria, 2003; 171–177.

15. Garolera D, Lopez CM, Carol I, Papanastasiou P. Micromechanical analysis of the rock sanding problem. *Journal of the Mechanical Behaviour of Materials* 2005; **16**(1–2):45 – 53.
16. Caballero A, Lopez CM, Carol I. 3D meso-structural analysis od concrete specimens under uniaxial tension. *Fifth International Conference on Fracture Mechanics of Concrete and Concrete Structures (FRAMCOS-5)*, Vail, Colorado, 2004; 329 – 336.
17. Caballero A, Carol I, Lopez CM. 3D fracture analysis of concrete under uniaxial tension and compression solicitacion. *Complas VIII Proceedings*, Oñate *et al*. (eds), Part 1. CIMNE Publications: Barcelona, 2005; 423 – 426.
18. Ortiz M, Pandolfi A. Finite-deformation irreversible cohesive elements for the three-dimensional crack-propagation analysis. *International Journal for Numerical Methods in Engineering* 1999; **44**(9):1267–1282.
19. Ladevèze P, Maunder EAW. A general method for recovering equilibrating element tractions. *Computer Methods in Applied Mechanics and Engineering* 1996; **137**:111–151.
20. Carol I, Prat P, Bažant Z. New explicit microplane model for concrete: theoretical aspects and numerical implementation. *International Journal of Solids and Structures* 1992; **29**:1173–1191.
21. Riggs HR, Tessler A, Chu H. Continuous stress recovery in finite element analysis. *Computer Methods in Applied Mechanics and Engineering* 1997; **143**:299 – 316.
22. Zienkiewicz OC, Zhu JZ. A simple error estimator and adaptive procedure for practical engineering analysis. *International Journal for Numerical Methods in Engineering* 1987; **24**:337 – 357.
23. Hughes TJR. *Finite Element Method—Linear Static and Dynamic Finite Element Analysis.* Prentice-Hall: Englewood Cliffs, NJ, 1987.
24. Boroomand B, Zienkiewicz OC. Recovery by equilibrium patches. *International Journal for Numerical Methods in Engineering* 1997; **40**:137–164.